



Article

Hybrid High-Order and Fractional-Order Total Variation with Nonlocal Regularization for Compressive Sensing Image Reconstruction

Lijia Hou , Yali Qin *, Huan Zheng, Zemin Pan , Jicai Mei and Yingtian Hu

College of Information Engineering, Zhejiang University of Technology, Hangzhou 310023, China; wohoulijia@163.com (L.H.); zhenghuan@zjut.edu.cn (H.Z.); pzm_zjut@163.com (Z.P.); 2111703012@zjut.edu.cn (J.M.); huyt@zjut.edu.cn (Y.H.)

* Correspondence: yqlin@zjut.edu.cn

Abstract: Total variation often yields staircase artifacts in the smooth region of the image reconstruction. This paper proposes a hybrid high-order and fractional-order total variation with nonlocal regularization algorithm. The nonlocal means regularization is introduced to describe image structural prior information. By selecting appropriate weights in the fractional-order and high-order total variation coefficients, the proposed algorithm makes the fractional-order and the high-order total variation complement each other on image reconstruction. It can solve the problem of non-smooth in smooth areas when fractional-order total variation can enhance image edges and textures. In addition, it also addresses high-order total variation alleviates the staircase artifact produced by traditional total variation, still smooth the details of the image and the effect is not ideal. Meanwhile, the proposed algorithm suppresses painting-like effects caused by nonlocal means regularization. The Lagrange multiplier method and the alternating direction multipliers method are used to solve the regularization problem. By comparing with several state-of-the-art reconstruction algorithms, the proposed algorithm is more efficient. It does not only yield higher peak-signal-to-noise ratio (PSNR) and structural similarity (SSIM) but also retain abundant details and textures efficiently. When the measurement rate is 0.1, the gains of PSNR and SSIM are up to 1.896 dB and 0.048 dB respectively compared with total variation with nonlocal regularization (TV-NLR).

Keywords: total variation; high-order; fractional-order; nonlocal means regularization; staircase artifact; the alternating direction multipliers



Citation: Hou, L.; Qin, Y.; Zheng, H.; Pan, Z.; Mei, J.; Hu, Y. Hybrid High-Order and Fractional-Order Total Variation with Nonlocal Regularization for Compressive Sensing Image Reconstruction. *Electronics* **2021**, *10*, 150. <https://doi.org/10.3390/electronics10020150>

Received: 11 December 2020

Accepted: 7 January 2021

Published: 12 January 2021

Publisher's Note: MDPI stays neutral with regard to jurisdictional claims in published maps and institutional affiliations.



Copyright: © 2021 by the authors. Licensee MDPI, Basel, Switzerland. This article is an open access article distributed under the terms and conditions of the Creative Commons Attribution (CC BY) license (<https://creativecommons.org/licenses/by/4.0/>).

1. Introduction

Compressive sensing (CS) [1,2] has been successfully applied in signal acquiring, processing, and compression. By exploiting the redundancy that existed in a signal, CS conducts sampling, and compression at the same time. CS theory demonstrates that a signal can be reconstructed with high probability when it exhibits sparse representation in some transformation domain, which has been widely used in many fields, such as single-pixel imaging [3], remote sensing imaging [4], and medical imaging [5].

Based on the CS theory, if an original signal $x \in R^N$ is sparse or after sparse transformation Ψ . The measured value $y = \Phi x, y \in R^M (M \ll N)$ can be obtained through the measurement matrix Φ . CS theory shows that when the sparse transformation matrix Ψ and the measurement matrix Φ satisfy the restricted isometry property (RIP) [6], the original signal x can be reconstructed by solving the following optimization problem

$$\min_x \|\Psi^T x\|_0 \quad s.t. \quad y = \Phi x, \quad (1)$$

where signal $\alpha = \Psi^T x$, α is the sparse coefficient after sparse transformation. $\|\cdot\|_0$ represents the l_0 norm. Since the solution of Equation (1) is an NP-hard problem, it can be solved by the approximate form l_1 norm

$$\min_x \|\Psi^T x\|_1 \quad s.t. \quad y = \Phi x. \quad (2)$$

The above-constrained problem can be constructed by the Lagrangian multiplier method to an unconstrained problem

$$\tilde{x} = \arg \min_x \{ \|y - \Phi x\|_2^2 + \lambda \|\Psi^T x\|_1 \}, \quad (3)$$

where $\|y - \Phi x\|_2^2$ is a cost function, λ is the Lagrangian parameter. Since prior characteristics exist in natural images generated by natural light imaging, the optimization problem of image compression sensing can be expressed as

$$\tilde{u} = \arg \min_u \{ \|y - \Phi u\|_2^2 + \lambda R(u) \}, \quad (4)$$

where u is a 2D image. $R(u)$ represents a regularization term representing prior information of an image.

The current CS recovery algorithms explore the prior knowledge that a natural image is sparse in some domains, such as discrete cosine transform (DCT) [7], wavelets [8], and gradient-domain utilized by total variation (TV) model [9,10]. Image sparse representation is a key factor to affect image reconstruction quality. Despite high effectiveness in image CS recovery, the TV-based [11] algorithms cannot recover the fine details and textures, reconstructed images suffer from undesirable staircase artifact. This problem has sparked numerous studies in designing regularizers that could efficiently suppress the staircase artifacts while retaining sharp edges. To overcome this drawback, a weighted total variation [12] is proposed to improve the sparsity of the TV norm. Furthermore, an improved total variation by intraprediction is proposed [13]. Besides, total generalized variation (TGV) [14,15] is widely discussed, which is more precise in describing pixels variations in smooth regions, and thus reduces oil painting artifacts while still being able to preserve sharp edges. Except for these TV and its variants, there also exists some combination of TV (or TGV) and different waves, such as TV + wavelet [16] and TGV + shearlet [17]. However, the methods described above are improved on TV, there is still a staircase artifact effect in the results. Further, nonlocal means (NLM) [18] uses the similarity between the surrounding pixels of the image to perform weighted filtering, which effectively utilizes the non-local self-similarity. NLM is successfully applied in the CS image reconstruction, but it often results in the painting-like effect.

Recently, a class of fractional-order TV regularization models has received considerable interest and it is widely used in image denoising [19,20]. Adaptive weighted high-frequency iterative fractional-order TV is proposed, the high frequency gradient of an image is reweighted in iterations adaptively when using fractional-order TV [21]. Another conventional way to suppress the staircase artifact is to use a high-order TV regularization [22,23], there exists a high-order total variation minimization model that removes undesired artifacts for restoring blurry and noisy images [24]. High-order TV regularization can reconstruct piecewise linear regions, but high-order TV may also smooth out the image details, and it may reduce the ability of edges-preserving [23]. In order to make full use of image prior information as much as possible to construct a regularized model. A generalized hybrid non-convex variational regularization model [25] and unidirectional hybrid total variation with nonconvex low-rank regularization [26] have been proposed.

Motivated by the aforementioned studies, both the fractional-order TV and high-order TV can solve the problem of staircase artifacts, but fractional-order TV will cause non-smooth effects just like noise in smooth areas of the image. The ability of high-order TV to reduce the staircase effect is not very ideal since it may smooth the image details.

In this paper, a two-dimensional compressive sensing image reconstruction model based on hybrid high-order and fractional-order TV (HoFrTV) with nonlocal regularization is proposed. The proposed algorithm makes the fractional-order and the high-order TV complement each other on image reconstruction, which can effectively solve the problems caused by high-order and fractional-order TV. The proposed algorithm effectively reduces the problem of staircase artifacts while preserving the edges, and suppresses painting-like effects produced by nonlocal means regularization.

To effectively solve the proposed algorithm model, we introduce auxiliary variables to a construct constrained optimization problem in Section 2.2. We divide the proposed model into four subproblems to solve. These subproblems are fractional-order TV model, high-order TV model, nonlocal means regularization model, and the reconstructed image by iterative update respectively. The augmented Lagrangian method (ALM) and the alternating direction method of multipliers (ADMM) are incorporated to solve these problems. Each parameter of the Lagrangian function is optimized for the experiment results empirically. The experimental results show that the proposed algorithm outperforms the current state-of-the-art algorithms, the edges and details of the reconstructed image are more abundant, and the visual effect of the reconstructed image is better.

The remainder of this paper is organized as follows. Section 2 introduces the related regularization model and the proposed HoFrTV model. In Section 3, parameter selection and experimental results are presented. In Section 4, the conclusions are drawn.

2. The Proposed Algorithm Model

2.1. Regularization Model

2.1.1. Fractional-Order Total Variation Model

Fractional total variation can be regarded as the generalization of total variation composed of fractional orders. There are three widely used definitions of the model, including Riemann-Liouville (R-L), Grünwald-Letnikov (G-L), and Caputo model [27]. Here, we choose the G-L model because it is easier to implement for image reconstruction. The G-L model can be defined as

$${}_a D_t^\alpha f(t) = \lim_{h \rightarrow 0} \frac{1}{h^\alpha} \sum_{k=0}^{\lfloor \frac{t-a}{h} \rfloor} (-1)^k \binom{\alpha}{k} f(t - kh), \quad (5)$$

where α fractional order, t and a are the upper and lower boundaries of the independent variable respectively, and h is the differential step-size, $\binom{\alpha}{k}$ is the binomial coefficient

and defined as $\binom{\alpha}{k} = \frac{\Gamma(\alpha+1)}{\Gamma(k+1)\Gamma(\alpha-k+1)}$, where $\Gamma(\cdot)$ is the Gamma function. Without loss of generality, let u denote the image. The fractional-order total variation in the horizontal and vertical directions can be expressed as

$$[D^\alpha u] = ((D_h^\alpha u), (D_v^\alpha u)), \quad (6)$$

and

$$\begin{cases} (D_h^\alpha u) = \sum_{k=0}^{K-1} (-1)^k \binom{\alpha}{k} u(i-k, j) \\ (D_v^\alpha u) = \sum_{k=0}^{K-1} (-1)^k \binom{\alpha}{k} u(i, j-k) \end{cases}, \quad (7)$$

where i and j denote the pixel in the i -th row and the j -th column of an $N \times N$ size image. $K \geq 3$ is the number of items involved in the computation of the fractional-order derivative, which is usually set as $K = N$. Based on this definition, the fractional-order semi-norm is defined as

$$\|D^\alpha u\|_{FrTV} = \sum_{i=1}^N \sum_{j=1}^N \sqrt{[(D_h^\alpha u)]^2 + [(D_v^\alpha u)]^2}. \quad (8)$$

2.1.2. High-Order Total Variation Model

On the basis of the first-order total variation operators of the image, we can obtain the high-order total variation, defined as

$$D^2u = (D_{vv}u, D_{vh}u, D_{hv}u, D_{hh}u) \\ \|D^2u\| = \sqrt{|D_{vv}u|^2 + |D_{vh}u|^2 + |D_{hv}u|^2 + |D_{hh}u|^2} \quad (9)$$

where $(D_{vv}u)$, $(D_{vh}u)$, $(D_{hv}u)$, and $(D_{hh}u)$ are high-order total variation operators in the horizontal and vertical directions, respectively. The high-order total variation can be seemed as performing the differential operation again on the first-order total variation.

2.1.3. Nonlocal Mean Regularization Model

The pixels in the image can be estimated by the weighted average of the surrounding pixels of similar neighborhoods in the similar neighborhood of the search window, which can be expressed as follows

$$\hat{u}_i = \sum_{j \in \Omega} w_{i,j} u_j, \quad (10)$$

where Ω is a search window area $D_s \times D_s$. let u_i and u_j denote the central pixel of similar neighborhood window $d_s \times d_s$ respectively. The weight of u_j to u_i , denoted by $w_{i,j}$, which is determined by the similarity of the pixels in a similar neighborhood window. It can be calculated by the Gaussian l_2 distance between pixels in the neighborhood window. It can be written in the following form

$$w_{i,j} = \frac{1}{c} \exp\left(-\frac{\|u_j - u_i\|_2^2}{h^2}\right). \quad (11)$$

Specifically, assume that u_j lies in the search window of u_i . The neighborhood window centered on the central pixel u_j can slide in the search window to calculate the similarity between two neighboring windows. h is the factor controlling the Gaussian kernel and c is the normalization constant. Applying nonlocal regularization in the CS reconstruction process, furthermore, it can be rewritten in a matrix form as

$$R(u) = \|u - Wu\|_2^2, \quad (12)$$

here, W represents a matrix composed of $w_{i,j}$ in Equation (10), let $R(u)$ denote nonlocal regularization term. When calculating the second norm, vectorizing the elements in the norm is employed and then the second norm of the vectorized matrix is calculated.

2.2. The Proposed Algorithm Model

Incorporating Equations (8), (9), and (12) into the CS optimization problem jointly, the proposed hybrid high-order and fractional-order total variation with nonlocal regularization model image CS recovery algorithm are formulated as

$$\arg \min_u \tau \|D^\alpha u\|_1 + \varepsilon \|D^2u\|_1 + \beta \|u - Wu\|_2^2 \quad s.t. \quad y = \Phi u. \quad (13)$$

Using variable splitting, we introduce auxiliary variables and change Equation (13) to a constrained optimization problem

$$\arg \min_u \tau \|w\|_1 + \varepsilon \|v\|_1 + \beta \|z - Wu\|_2^2 \\ s.t. \quad D^\alpha u = w, D^2u = v, u = z, y = \Phi u \quad (14)$$

where τ and ε control the weights of fractional-order and high-order total variation. Note that the problem of Equation (14) is quite difficult to solve directly due to the non-

differentiability and non-linearity of the combined regularization terms. An augmented Lagrangian based approach is developed to solve the problem

$$L_A(w, v, z, u) = \tau(\|w\|_1 - \gamma_1^T(D^\alpha u - w) + \frac{\mu_1}{2}\|D^\alpha u - w\|_2^2) + \varepsilon(\|v\|_1 - \gamma_2^T(D^2 u - v) + \frac{\mu_2}{2}\|D^2 u - v\|_2^2) + \frac{\mu_3}{2}\|\Phi u - y\|_2^2 - \gamma_3^T(\Phi u - y) + \beta\|z - Wz\|_2^2 - \gamma_4^T(u - z) + \frac{\mu_4}{2}\|u - z\|_2^2 \quad (15)$$

where $\mu_1, \mu_2, \mu_3, \mu_4$, and β are regularization parameters associated with the quadratic penalty terms. $\gamma_1, \gamma_2, \gamma_3$, and γ_4 are the Lagrange multipliers associated with the constraints of Equation (15). The idea of using ADMM is to find a saddle point of $L_A(w, v, z, u)$ which is the solution to the original problem in Equation (13). It can minimize the augmented Lagrangian function $L_A(w, v, z, u)$ alternately, the problem in Equation (15) is decomposed into the four subproblems. We investigated the subproblems one by one.

2.2.1. w and v Subproblems

Given v, z , and u , the optimization problem associated with w can be expressed as

$$\tilde{w} = \underset{w}{\operatorname{argmin}} \tau(\|w\|_1 - \gamma_1^T(D^\alpha u - w) + \frac{\mu_1}{2}\|D^\alpha u - w\|_2^2). \quad (16)$$

According to Lemma 2 [28], the closed solution form of Equation (16) is

$$\tilde{w} = \max \tau \left\{ \left| D^\alpha u - \frac{\gamma_1}{\mu_1} \right| - \frac{1}{\mu_1}, 0 \right\} \cdot \operatorname{sgn}(D^\alpha u - \frac{\gamma_1}{\mu_1}). \quad (17)$$

When solving v subproblem, given w, v and z , similarly, the v subproblem becomes

$$\tilde{v} = \underset{v}{\operatorname{argmin}} \varepsilon(\|v\|_1 - \gamma_2^T(D^2 u - v) + \frac{\mu_2}{2}\|D^2 u - v\|_2^2). \quad (18)$$

Same as w subproblems, the closed solution form of (18) can write as

$$\tilde{v} = \max \varepsilon \left\{ \left| D^2 u - \frac{\gamma_2}{\mu_2} \right| - \frac{1}{\mu_2}, 0 \right\} \cdot \operatorname{sgn}(D^2 u - \frac{\gamma_2}{\mu_2}). \quad (19)$$

2.2.2. u Subproblems

Fixed w, v , and z , u subproblems is equivalently expressed as

$$\tilde{u} = \underset{u}{\operatorname{argmin}} \tau(-\gamma_1^T(D^\alpha u - \tilde{w}) + \frac{\mu_1}{2}\|D^\alpha u - \tilde{w}\|_2^2) + \varepsilon(-\gamma_2^T(D^2 u - \tilde{v}) + \frac{\mu_2}{2}\|D^2 u - \tilde{v}\|_2^2) + \frac{\mu_3}{2}\|\Phi u - y\|_2^2 - \gamma_3^T(\Phi u - y) - \gamma_4^T(u - z) + \frac{\mu_4}{2}\|u - z\|_2^2 \quad (20)$$

We can see that the problem in Equation (20) is a quadratic function optimization problem. To reduce the calculation, the gradient descent method was used

$$\tilde{u} = u - \eta \cdot d, \quad (21)$$

η is the step size. u can be reconstructed by every iterative update, d indicates its gradient,

$$d = \tau(D^\alpha)^T(\mu_1 D^\alpha - \gamma_1 - \mu_1 \tilde{w}) + \varepsilon(D^2)^T(\mu_2 D^2 - \gamma_2 - \mu_2 \tilde{v}) - \gamma_4 + \mu_4(u - z) + \Phi^T(\mu_3(\Phi u - y) - \gamma_3), \quad (22)$$

where $\eta = \operatorname{abs}(d^T d / d^T G d)$ is the optimal step and $G = \mu_1(D^\alpha)^T D^\alpha + \mu_4 I + \mu_3 \Phi^T \Phi$.

2.2.3. z Subproblems

Similar to other subproblems, z subproblems becomes

$$\tilde{z} = \arg \min_z \beta \|z - Wz\|_2^2 - \gamma_4^T (\tilde{u} - z) + \frac{\mu_4}{2} \|\tilde{u} - z\|_2^2. \quad (23)$$

According to [18], the Equation (23) can be further transformed into

$$\min_z \frac{1}{2} \|z - r\|_2^2 + \frac{\beta}{\mu_4} \|z - Wz\|_2^2, \quad (24)$$

where $r = (\tilde{u} - \frac{\gamma_4}{\mu_4})$, r can be regarded as an approximation of z . Since the weight matrix W represents the nonlocal means operator, the Equation (24) can be rewritten as

$$\min_z \frac{1}{2} \|z - r\|_2^2 + \frac{\beta}{\mu_4} \|z - Wr\|_2^2. \quad (25)$$

Setting the gradient of the Equation (25) to zero, we acquire the closed-form solution as follows

$$\tilde{z} = \frac{\mu_4 r + 2\beta W r}{\mu_4}. \quad (26)$$

Finally, the Lagrange multipliers are updated by the following

$$\begin{cases} \gamma_1^{k+1} = \gamma_1^k - \mu_1 (D^\alpha u^{k+1} - w^{k+1}) \\ \gamma_2^{k+1} = \gamma_2^k - \mu_2 (D^2 u^{k+1} - w^{k+1}) \\ \gamma_3^{k+1} = \gamma_3^k - \mu_3 (\Phi u^{k+1} - y) \\ \gamma_4^{k+1} = \gamma_4^k - \mu_4 (u^{k+1} - z^{k+1}) \end{cases}. \quad (27)$$

Once we obtained an efficient solution for each separated subproblem, the overall algorithm will be more efficient to get better reconstruction. Given all the derivations above, the specific implementation process of the proposed algorithm is described in Algorithm 1.

Algorithm 1 HoFrTv algorithm.

Input: The observed measurement y , the measurement matrix Φ and $\mu_1, \mu_2, \mu_3, \mu_4, \beta$

Initialization: $u_0 = \Phi^T y$, $\gamma_1 = \gamma_2 = \gamma_3 = \gamma_4 = 0$, $w_0 = v_0 = z_0 = 0$

While Outer iteration unsatisfied **do**

While Inner iteration unsatisfied **do**

 Solve w subproblem via Equation (17)

 Solve v subproblem via Equation (19)

 Solve u subproblem via Equation (21)

 Compute the weight w_{ij} via Equation (11)

 Solve z subproblem via Equation (26)

end while

 Update multipliers via Equation (27)

end while

Output: the reconstructed image

3. Experimental Results and Discussion

In this section, the experimental results are presented to demonstrate the performance of the proposed algorithm HoFrTv model. In our implementation, we chose the USC-SIPI image database, which is a collection of digitized images. The database was maintained primarily to support research in image processing, image analysis, and machine vision. Ten images were selected for verification, the original images are shown in Figure 1.

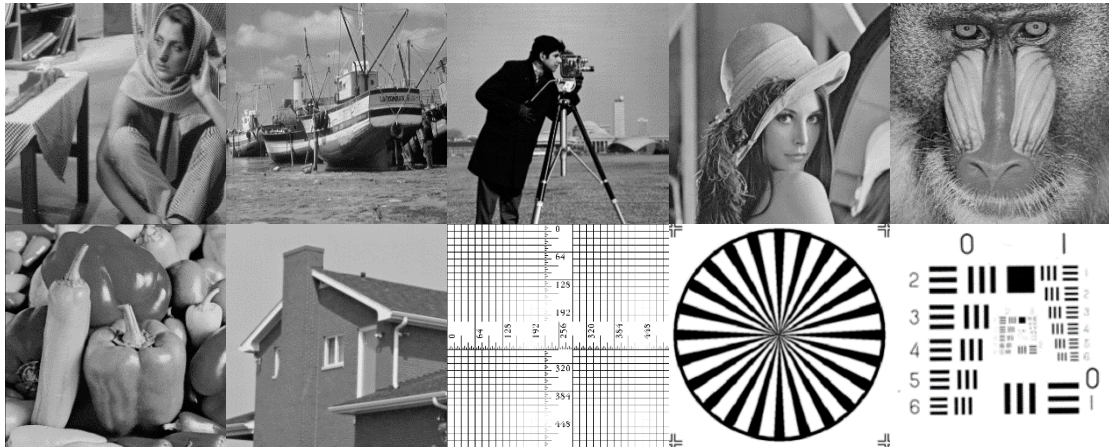


Figure 1. Test images.

Reconstructed image quality was measured using the peak signal-to-noise ratio (PSNR) and the structure similarity (SSIM) [29]. The calculation expression is as follows

$$\text{PSNR} = 20 \log_{10} \frac{R}{\text{RMSE}} \quad (28)$$

$$\text{RMSE} = \sqrt{\frac{1}{MN} \sum_{i=1}^M \sum_{j=1}^N (u_{ij} - \tilde{u}_{ij})^2} \cdot$$

The root mean square error is the arithmetic square root of the mean square error, it can measure the deviation between the reconstructed image and the original image. Where \tilde{u}_{ij} and u_{ij} denote the pixel values of the reconstructed image and the original image, R is the maximum value of the image gray level range. SSIM is defined as

$$\text{SSIM} = \frac{(2\mu_x\mu_y + C_1)(2\sigma_{xy} + C_2)}{(\mu_x^2 + \mu_y^2 + C_1)(\sigma_x^2 + \sigma_y^2 + C_2)}, \quad (29)$$

where μ_x and μ_y are the mean value of the reconstructed image and the original image. σ_x and σ_y are the standard deviations of the reconstructed image and the original image. C_1 and C_2 are small positive numbers to avoid $\mu_x^2 + \mu_y^2$ and $\sigma_x^2 + \sigma_y^2$ being zero, and

$$\sigma_{xy} = \left(\frac{1}{N-1}\right)^2 \sum_{i=1}^N \sum_{j=1}^N (u_{ij} - \mu_x)(\tilde{u}_{ij} - \mu_y). \quad (30)$$

The stopping criterion for all of the algorithms tested was set to

$$\frac{\|\tilde{u}^t - \tilde{u}^{t+1}\|_2}{\|\tilde{u}^{t+1}\|_2} \leq 10^{-3}, \quad (31)$$

where \tilde{u}^{t+1} and \tilde{u}^t are the restored images at the current iterate and previous iterate respectively.

3.1. Parameter Selection

Since τ and ε were related to the weights of fractional-order and high-order total variation, the respective ranges of τ and ε were greater than 0 and less than 1. We constrained the summation of these two weights to be 1 in our proposed algorithm model. In the following content, we analyzed the influence of high-order and fractional-order weights parameters on the reconstructed results.

3.1.1. The Influence of High-Order

This subsection discusses the influence of high-order TV when Equation (14) does not exist in fractional-order, which means that the fractional-order is the traditional total

variation. In order to investigate its effect, experiments were implemented with different weight parameters ε to high-order TV, the weights parameters value range was greater than 0 and less than 1. We randomly selected Lena image, the results are shown in Table 1.

Table 1. Peak signal-to-noise ratio (PSNR) (dB)/structural similarity (SSIM) results for the different ε for Lena image.

ε	Measurement Rates				
	0.1	0.15	0.2	0.25	0.3
0.1	26.539/0.801	28.398/0.845	29.526/0.875	30.699/0.895	31.733/0.916
0.2	26.721/0.807	28.411/0.846	29.545/0.877	30.799/0.897	31.797/0.916
0.3	26.790/0.809	28.485/0.853	29.696/0.879	30.905/0.900	31.896/0.918
0.4	26.949/0.814	28.537/0.853	29.706/0.880	30.957/0.903	32.023/0.920
0.5	26.984/0.815	28.681/0.854	29.805/0.882	31.059/0.905	32.140/0.922
0.6	27.320/0.824	28.763/0.860	29.947/0.886	31.158/0.907	32.235/0.924
0.7	27.235/0.823	28.891/0.856	30.030/0.888	31.277/0.910	32.401/0.927
0.8	26.670/0.803	28.911/0.861	30.130/0.895	31.312/0.912	32.503/0.929
0.9	26.671/0.813	28.677/0.860	30.059/0.893	30.953/0.901	32.583/0.930

From Table 1, with the parameter ε increasing, the higher the parameter ε was, the better the result of reconstruction. This is due to high-order TV that can effectively reduce the stair casing artifacts in the reconstructed image. According to the experimental results, when parameter ε was between 0.6 and 0.9, the reconstruction results could achieve stable results. So, the parameter ε value range could be selected from 0.6 to 0.9. According to the experiment in the database, we could make appropriate selection values according to different images. In our experiments, we set $\varepsilon = 0.7$ and $\tau = 0.3$ to balance the results.

3.1.2. The Influence of Fractional-Order

In this experiment, α is the fractional-order. The effect of this parameter on the image reconstruction performance was tested without high-order TV in Equation (14), ranging from 0.5 to 2. Image Lena was tested in the experiment. The results are shown in Table 2.

Table 2. PSNR (dB)/SSIM results for the different fractional-order for Lena image.

α	Measurement Rates				
	0.1	0.15	0.2	0.25	0.3
0.5	20.427/0.580	22.578/0.651	26.361/0.718	25.553/0.758	26.919/0.801
0.7	24.061/0.720	25.876/0.773	27.534/0.822	28.800/0.854	29.841/0.879
0.9	26.065/0.782	27.729/0.828	28.988/0.860	30.252/0.888	31.362/0.908
1	26.483/0.794	28.187/0.839	29.379/0.869	30.567/0.894	31.595/0.912
1.1	26.823/0.803	28.305/0.842	29.631/0.874	30.727/0.897	31.775/0.914
1.3	27.021/0.810	28.506/0.847	29.833/0.879	30.848/0.900	31.865/0.917
1.5	26.996/0.810	28.604/0.852	30.092/0.887	31.024/0.903	32.071/0.922
1.7	26.956/0.809	28.591/0.853	30.125/0.889	31.093/0.906	32.074/0.924
1.9	26.858/0.806	28.561/0.854	30.119/0.889	31.191/0.908	32.252/0.925
2.0	26.700/0.801	28.526/0.852	30.108/0.889	31.250/0.908	32.282/0.926

From Table 2, we could see that when $\alpha < 1$, the reconstructed results were poor. The reason is fractional-order TV loses more details and textures. When $\alpha = 1$, fractional-order TV converts to traditional TV. When $\alpha > 1$, the larger the parameter α is, the better the textures and image details. We can see that the PSNR at $\alpha = 1$ is lower than the PSNR at $\alpha > 1$. We can select the fractional-order α between $\alpha = 1.3$ and $\alpha = 2$. However, when a value of α is too close to 2, the frequency of textures would be enhanced excessively that becomes a kind of noise. Finally, to achieve a good trade-off, in our experiments, we set $\alpha = 1.7$ to balance the results.

3.1.3. The Influence of Non-Local Mean Regularization Kernel Window and Search Window

Non-local means regularization indicates the estimated value of the current pixel obtained by the weighted average of the pixels in the image that have a similar neighborhood structure. There is no doubt that the radius of the neighborhood kernel window and the radius of the neighborhood search window were vital to the experiment. If their values are too small, the self-similarity of the image cannot be fully utilized, and the characteristics of the non-local means cannot be used fully. If their values are too large, the image search area will become larger and the time will be longer, which leads to the fact that the algorithm efficiency will be lower. There are different kernel windows to search window ratio ($k:s$) result values for different measurement rates in Table 3. Figure 2 shows the PSNR and time curves with measurement rates = 0.1 and 0.15 for different $k:s$. We can see from Table 3 and Figure 2 that the performance was the best when $k:s$ was 3:7 considering from time and PSNR. Therefore, the kernel window and search window were set to be 3 and 7 in the following experiments.

Table 3. PSNR (dB)/SSIM and time (s) results for the different $k:s$ ratios.

Rates	PSNR (dB)/SSIM and Time (s)			
	$k:s = 1:3$	$k:s = 3:7$	$k:s = 5:11$	$k:s = 7:15$
0.1	26.448/0.793 198	27.460/0.828 289	27.463/0.828 901	27.510/0.832 3715
0.15	28.553/0.854 116	29.108/0.870 440	29.214/0.870 831	29.161/0.872 3996
0.2	30.097/0.888 93	30.379/0.896 366	30.525/0.896 1327	30.837/0.902 2439
0.25	31.183/0.908 120	31.612/0.916 311	32.158/0.916 1039	32.034/0.921 3639
0.3	32.208/0.925 99	32.821/0.933 208	32.958/0.933 1181	32.869/0.933 3610

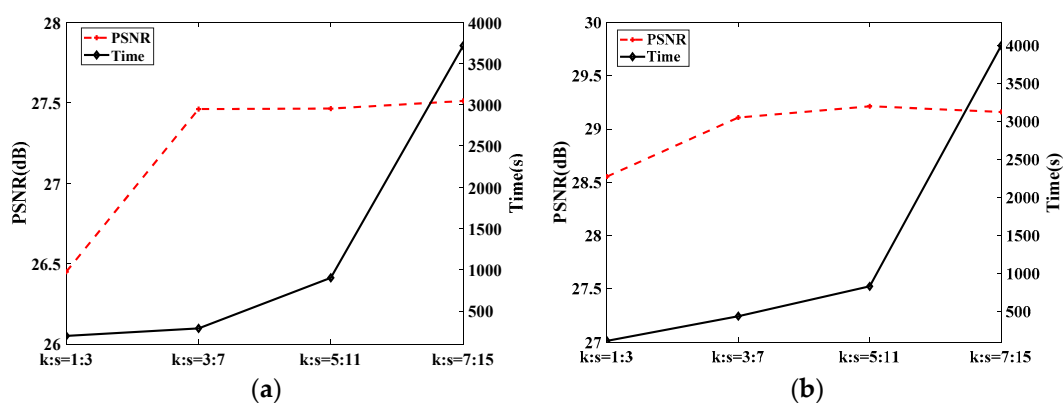


Figure 2. The PSNR and time curves for different $k:s$ ratios: (a) measurement rates = 0.1 and (b) measurement rates = 0.15.

3.2. Parameter Verification

3.2.1. Verify Fractional Order Existence Performance

According to Section 3.1, we set fractional-order $\alpha = 1.7$ in this experiment, in order to verify the validity of fractional-order existence. On the basis of Section 3.1.1, the fractional-order $\alpha = 1.7$ was added. The test image selection was the same as the previous tested image Lena. The results are shown in Table 4.

Table 4. PSNR (dB)/SSIM results for the different ε for the Lena image.

ε	Measurement Rates				
	0.1	0.15	0.2	0.25	0.3
0.1	27.016/0.811	28.731/0.856	30.155/0.890	31.209/0.910	32.204/0.925
0.2	27.097/0.814	28.795/0.858	30.190/0.891	31.286/0.911	32.241/0.925
0.3	27.186/0.817	28.852/0.859	30.238/0.892	31.348/0.912	32.292/0.926
0.4	27.283/0.820	28.939/0.862	30.291/0.893	31.422/0.913	32.365/0.927
0.5	27.407/0.824	29.056/0.864	30.358/0.895	31.469/0.914	32.450/0.928
0.6	27.497/0.827	29.159/0.867	30.396/0.896	31.581/0.916	32.525/0.929
0.7	27.600/0.831	29.222/0.869	30.400/0.897	31.610/0.917	32.636/0.931
0.8	27.405/0.828	29.139/0.867	30.347/0.894	31.731/0.919	32.714/0.932
0.9	26.883/0.810	28.967/0.864	30.156/0.892	31.499/0.913	32.713/0.932

Comparing Table 1 with Table 4, we could see that the image reconstructed results in Table 4 were overall higher. The performance of fractional-order existence was better than that without fractional-order.

3.2.2. Verify High-Order Existence Performance

Similarly, in this experiment. In Section 3.1.2, the weight of high-order TV was 0.7. In order to verify the validity of high-order existence. On the basis of Section 3.1.2, the high-order was added. The test image was Lena. The results are shown in Table 5.

Table 5. PSNR (dB)/SSIM results for the different fractional-order for the Lena image.

α	Measurement Rates				
	0.1	0.15	0.2	0.25	0.3
0.5	21.541/0.626	26.831/0.810	28.642/0.856	29.952/0.885	31.306/0.909
0.7	25.537/0.762	28.106/0.841	29.492/0.872	30.613/0.895	31.920/0.917
0.9	26.482/0.791	28.523/0.854	30.015/0.885	31.189/0.908	32.437/0.926
1	26.745/0.800	28.611/0.853	30.113/0.886	31.337/0.909	32.524/0.927
1.1	27.086/0.814	28.725/0.857	30.195/0.887	31.367/0.91	32.553/0.928
1.3	27.495/0.826	28.996/0.866	30.328/0.892	31.450/0.912	32.556/0.928
1.5	27.552/0.829	28.946/0.865	30.319/0.894	31.445/0.912	32.611/0.929
1.7	27.493/0.829	28.977/0.866	30.347/0.894	31.489/0.916	32.714/0.932
1.9	27.190/0.822	29.053/0.868	30.357/0.895	31.617/0.918	32.769/0.932
2.0	26.975/0.820	28.947/0.867	30.500/0.899	31.787/0.920	32.852/0.933

From comparing Table 2 with Table 5, we could see that the performance of high-order existence was better than that without high-order by comparing data one by one.

In order to verify the effect of the proposed algorithm, we gave the visual comparison of different TV modes in algorithms to test images Lena and Peppers. From Figures 3 and 4, traditional TV with nonlocal means regularization in Figures 3a and 4a usually produced undesirable staircase artifact and painting-like effects. Even though fractional-order TV in Figures 3b and 4b could enhance image edges and textures, it could cause non-smooth of smooth areas. Although, the high-order TV in Figures 3c and 4c was capable of alleviating the problem caused by traditional TV, still smoothed out the details of the image, which led to the fact that the effect was not ideal. In Figures 3d and 4d, this was obvious that our proposed algorithm made the fractional-order and the high-order TV complement each other on image reconstruction. From the figures, we could see that our proposed algorithm preserved image edges and textures more effectively, and could alleviate the staircase artifact and painting-like effects produced by nonlocal means regularization.

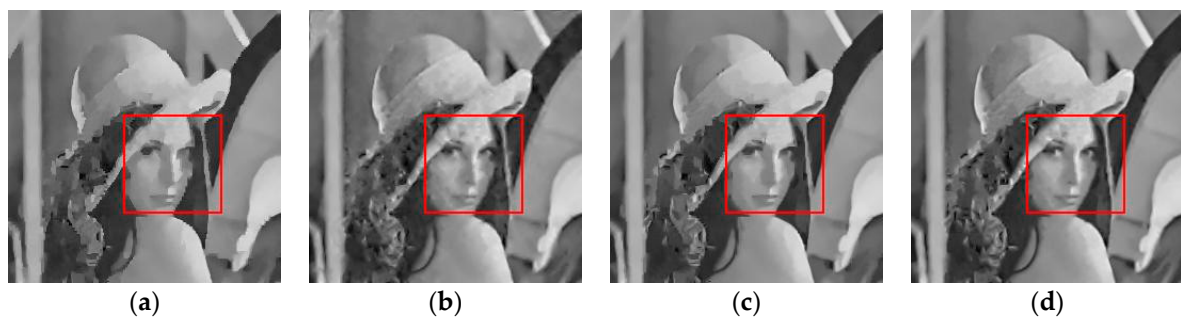


Figure 3. Lena image measurement rate = 0.1. (a) Reconstructed image by traditional TV, PSNR = 26.272 dB, and SSIM = 0.789; (b) Reconstructed image by only fractional-order (order = 1.7) TV, PSNR = 26.956 dB, and SSIM = 0.809. (c) Reconstructed image by only higher-order (weight = 0.7) TV, PSNR = 26.670 dB, and SSIM = 0.803. (d) Reconstructed image by high-order (weight = 0.7) and fractional-order (order = 1.7) TV, PSNR = 27.493 dB, and SSIM = 0.829.

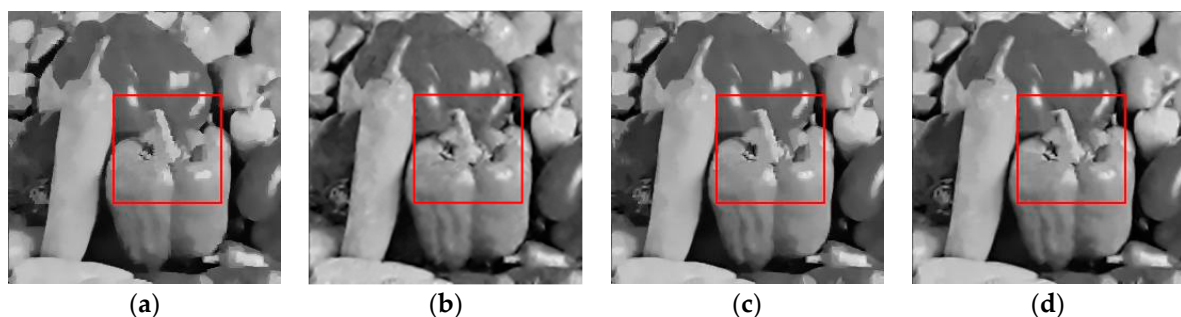


Figure 4. Peppers image measurement rate = 0.1. (a) Reconstructed image by traditional TV, PSNR = 26.601 dB, and SSIM = 0.829; (b) reconstructed image by only fractional-order (order = 1.7) TV, PSNR = 27.748 dB, and SSIM = 0.847; (c) reconstructed image by only higher-order (weight = 0.7) TV, PSNR = 26.787 dB, and SSIM = 0.828; (d) reconstructed image by high-order (weight = 0.7) and fractional-order (order = 1.7) TV, PSNR = 28.497 dB, and SSIM = 0.868.

3.3. Comparison to Other Reconstruction Algorithms

In this experiment, we compared the proposed method with several state-of-the-art algorithms: TVNLR [18], BCS-TV [21], TVAL3 [28], and two non-TV based algorithms: BCS-SPL [30] and MH-BCS [31]. In order to reduce the computational complexity and memory requirements. Images were divided into non-overlapping blocks of size 32×32 for all algorithms. Table 6 displays their PSNR and SSIM values with the growth of the measurement rates for each image. We added additional test images and reconstruction results in the Appendix A. Figures 5 and 6 display PSNR and SSIM values respectively with the growth of the measurement rates for two images. From Table 6 and Figures 5 and 6, it can be seen that the HoFrTV algorithm performed best for the images at different measurement rates. The visual quality of the reconstructed images was used to further verify the effectiveness of the proposed algorithm. To compare the results visually, Figures 7 and 8 optionally display some reconstructed images and local enlargements obtained using the different algorithms with a 0.2 measurement rate. We can clearly see that the visual quality of the images recovered by HoFrTV was better than that of others. HoFrTV could efficiently reconstruct fine details and textures while preserving sharp edges and avoid producing painting-like effects.

Table 6. The PSNR (dB)/SSIM results of various algorithms with different measurement rates.

Image	Algorithms	Measurement Rates				
		0.1	0.15	0.2	0.25	0.3
barbara	TV-NLR	24.926/0.723	26.458/0.781	27.236/0.807	27.970/0.832	29.113/0.859
	MH-BCS	25.605/0.740	27.162/0.798	28.103/0.815	29.126/0.853	30.015/0.853
	BCS-TV	24.215/0.681	25.560/0.738	26.585/0.778	27.421/0.807	28.167/0.830
	BCS-SPL	23.619/0.640	25.067/0.697	26.209/0.739	27.105/0.770	27.807/0.793
	TVAL3	23.563/0.664	25.814/0.751	26.812/0.788	27.480/0.810	28.335/0.834
	HoFrTV	25.706/0.758	27.253/0.807	28.304/0.834	29.317/0.861	30.211/0.879
boat	TV-NLR	24.136/0.674	25.553/0.746	26.475/0.782	27.509/0.819	28.350/0.847
	MH-BCS	24.322/0.682	25.879/0.745	27.170/0.796	28.198/0.831	29.011/0.851
	BCS-TV	23.190/0.623	24.691/0.702	26.013/0.758	27.156/0.800	28.152/0.834
	BCS-SPL	22.974/0.596	24.079/0.647	25.090/0.69	26.088/0.733	26.929/0.766
	TVAL3	23.393/0.631	25.035/0.716	26.421/0.773	27.403/0.810	28.445/0.84
	HoFrTV	24.465/0.699	26.258/0.774	27.523/0.816	28.615/0.851	29.953/0.881
cameraman	TV-NLR	24.561/0.794	26.245/0.838	27.356/0.864	28.904/0.890	29.968/0.909
	MH-BCS	24.366/0.751	26.672/0.813	27.939/0.853	29.229/0.875	30.892/0.912
	BCS-TV	23.613/0.761	25.196/0.807	26.652/0.844	27.864/0.871	28.910/0.892
	BCS-SPL	22.785/0.691	24.284/0.740	25.626/0.783	26.686/0.813	27.744/0.838
	TVAL3	23.169/0.727	25.442/0.817	26.741/0.850	28.018/0.877	29.284/0.900
	HoFrTV	25.102/0.813	26.992/0.858	28.791/0.887	30.244/0.907	31.600/0.926
house	TV-NLR	29.519/0.830	31.809/0.862	33.018/0.879	34.153/0.894	35.306/0.909
	MH-BCS	30.006/0.828	32.348/0.866	33.235/0.878	34.825/0.899	35.609/0.911
	BCS-TV	27.763/0.79	29.784/0.829	31.111/0.852	32.282/0.870	33.413/0.888
	BCS-SPL	26.627/0.742	28.104/0.770	29.815/0.814	31.059/0.838	31.464/0.840
	TVAL3	26.047/0.750	29.885/0.837	31.385/0.860	32.653/0.878	33.584/0.892
	HoFrTV	30.122/0.838	32.446/0.870	33.881/0.887	35.143/0.903	35.953/0.915
lena	TV-NLR	26.272/0.789	28.030/0.840	29.334/0.869	30.373/0.893	31.249/0.909
	MH-BCS	26.773/0.797	28.520/0.853	29.757/0.872	30.815/0.897	31.840/0.918
	BCS-TV	25.486/0.752	27.043/0.805	28.478/0.846	29.569/0.872	30.623/0.894
	BCS-SPL	24.56/0.689	26.142/0.742	27.423/0.784	28.473/0.816	29.443/0.841
	TVAL3	24.510/0.724	27.469/0.818	28.633/0.850	29.644/0.876	30.570/0.895
	HoFrTV	27.493/0.829	29.071/0.869	30.403/0.896	31.745/0.916	32.655/0.931
mandrill	TV-NLR	22.014/0.469	22.483/0.527	23.495/0.602	24.018/0.656	23.835/0.671
	MH-BCS	22.003/0.439	23.087/0.545	24.036/0.602	24.472/0.677	25.172/0.713
	BCS-TV	21.895/0.453	22.695/0.525	23.380/0.587	23.956/0.638	24.499/0.682
	BCS-SPL	22.069/0.449	22.701/0.504	23.264/0.559	23.695/0.599	24.186/0.639
	TVAL3	22.351/0.471	22.875/0.537	23.437/0.592	23.954/0.643	24.590/0.686
	HoFrTV	22.202/0.486	23.189/0.560	23.942/0.621	24.613/0.680	25.231/0.720
peppers	TV-NLR	26.601/0.829	29.119/0.879	30.762/0.906	32.295/0.925	33.845/0.940
	MH-BCS	26.929/0.805	29.035/0.854	30.614/0.884	31.739/0.902	32.938/0.918
	BCS-TV	25.802/0.790	28.270/0.850	30.001/0.882	31.432/0.905	32.799/0.924
	BCS-SPL	24.241/0.695	25.974/0.747	27.280/0.783	28.544/0.812	29.604/0.836
	TVAL3	24.515/0.767	27.949/0.853	29.709/0.885	31.198/0.908	32.467/0.924
	HoFrTV	28.497/0.868	30.991/0.906	32.755/0.929	34.309/0.944	35.732/0.954
ruler	TV-NLR	14.799/0.298	15.496/0.441	16.445/0.546	16.827/0.591	19.348/0.783
	MH-BCS	14.895/0.238	19.312/0.638	20.312/0.638	21.965/0.792	22.895/0.856
	BCS-TV	15.172/0.309	15.811/0.451	16.707/0.539	17.457/0.605	18.059/0.656
	BCS-SPL	15.870/0.401	16.550/0.497	17.493/0.595	18.365/0.661	19.141/0.712
	TVAL3	15.300/0.274	15.392/0.363	16.269/0.483	17.158/0.585	18.019/0.661
	HoFrTV	15.117/0.346	16.188/0.512	17.589/0.618	18.783/0.710	20.373/0.814
testpat	TV-NLR	16.397/0.723	19.372/0.831	19.440/0.792	24.283/0.929	26.333/0.959
	MH-BCS	16.819/0.779	19.135/0.828	20.142/0.856	22.379/0.879	24.798/0.956
	BCS-TV	15.981/0.709	18.798/0.820	21.241/0.888	23.224/0.932	24.934/0.960
	BCS-SPL	14.734/0.497	16.637/0.571	18.178/0.626	19.342/0.666	20.452/0.696
	TVAL3	14.834/0.613	17.719/0.752	19.338/0.799	22.402/0.900	24.212/0.936
	HoFrTV	17.799/0.803	22.762/0.910	26.047/0.944	28.512/0.965	30.191/0.970

Table 6. Cont.

Image	Algorithms	Measurement Rates				
		0.1	0.15	0.2	0.25	0.3
Resolutionchart	TV-NLR	20.726/0.880	25.863/0.950	27.620/0.966	32.921/0.982	35.516/0.988
	MH-BCS	18.511/0.707	20.473/0.783	22.234/0.819	24.008/0.862	25.640/0.886
	BCS-TV	9.173/0.578	9.649/0.6718	10.276/0.721	9.714/0.741	10.012/0.76
	BCS-SPL	16.213/0.550	18.068/0.607	19.215/0.627	20.384/0.654	21.410/0.676
	TVAL3	16.411/0.675	21.741/0.888	24.951/0.942	27.899/0.966	30.475/0.980
	HoFrTV	20.311/0.861	24.204/0.923	26.925/0.956	30.100/0.971	33.498/0.983

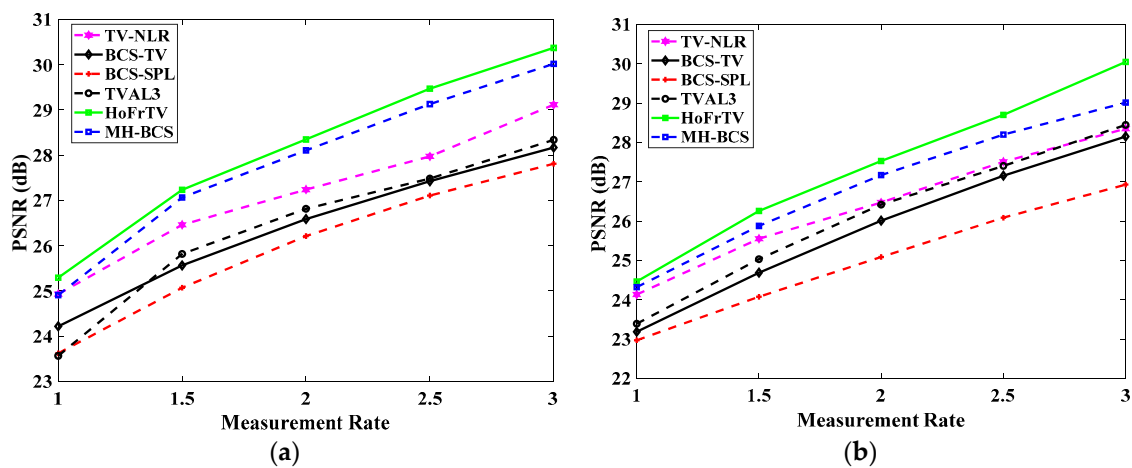


Figure 5. The PSNR curves of two images: (a) Barbara and (b) Boats.

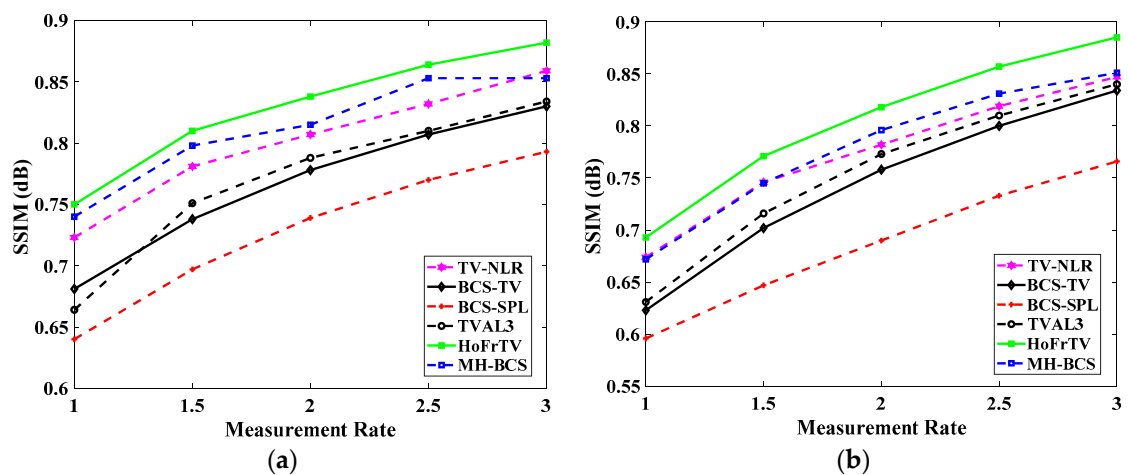


Figure 6. The SSIM curves of two images: (a) Barbara and (b) Boats.



Figure 7. Cont.

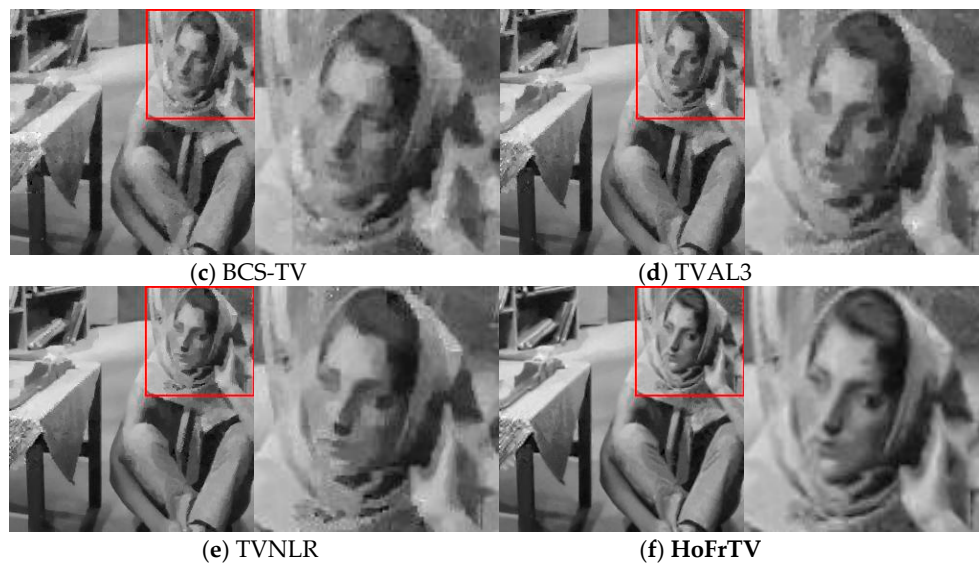


Figure 7. Reconstructed images (barbara) for measurement rate = 0.2 (a) PSNR = 28.103 dB and SSIM = 0.815; (b) PSNR = 27.748 dB and SSIM = 0.847; (c) PSNR = 26.585 dB and SSIM = 0.778; (d) PSNR = 26.812 dB and SSIM = 0.788; (e) PSNR = 27.237 dB and SSIM = 0.808; and (f) **PSNR = 28.304 dB and SSIM = 0.834.**

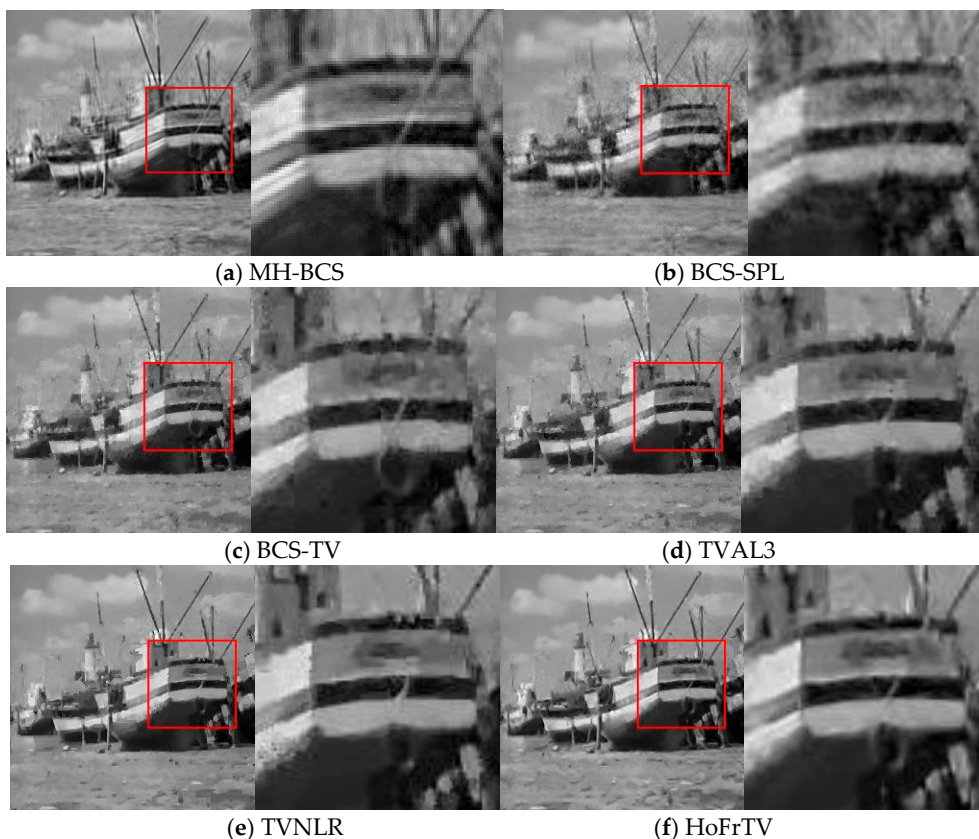


Figure 8. Reconstructed images (boat) for measurement rate = 0.2 (a) PSNR = 27.170 dB and SSIM = 0.796; (b) PSNR = 25.266 dB and SSIM = 0.697; (c) PSNR = 26.013 dB and SSIM = 0.758; (d) PSNR = 26.421 dB and SSIM = 0.774; (e) PSNR = 26.476 dB and SSIM = 0.783; and (f) **PSNR = 27.523 dB, and SSIM = 0.816.**

3.4. Computational Complexity

The experiments were performed under the MATLABR2018a environment with Intel Corei5-4200 CPU of 3.4 GHz and 4.0 GB RAM. Table 7 and Figure 9 give the time of

reconstructing image at different measurement rates. From this result, we could see that BCS-SPL, TVAL3, and MH-BCS were faster than the others. Comparing with TVNLR, HoFrTV, and BCS-TV, HoFrTV was faster than BCS-TV and slower than the TVNLR algorithm. It is because at each iteration needs to calculate the high-order and fractional-order total variation in the reconstruction process. However, the HoFrTV algorithm had higher reconstruction quality.

Table 7. Average reconstruction time(s).

Algorithms	BCS-SPL	TVAL3	MH-BCS	TV-NLR	HoFrTV	BCS-TV
Time (s)	Rate = 0.1	4.8	3.5	15.6	150.6	322.3
	Rate = 0.15	3.1	3.1	18.3	150.2	327.5
	Rate = 0.2	2.5	2.4	16.6	148.9	316.4
	Rate = 0.25	2.4	2.2	18.4	149.4	326.5
	Rate = 0.3	2.5	2.0	14.2	151.3	324.4
						775.6

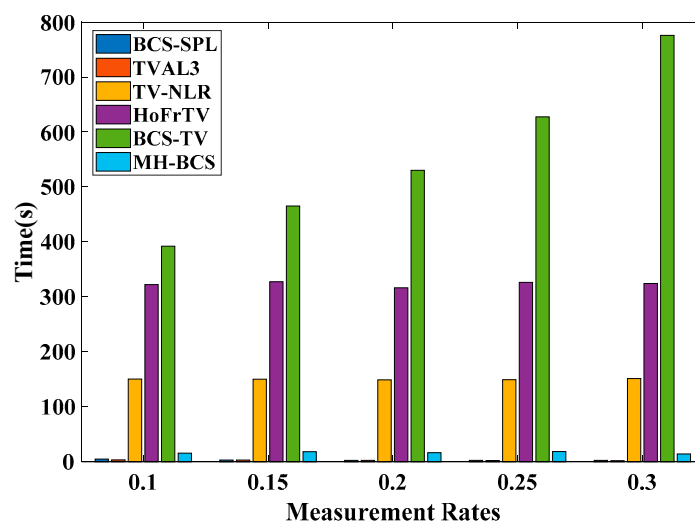


Figure 9. Average reconstruction time (s).

4. Conclusions

In this paper, a hybrid high-order and fractional-order total variation with nonlocal means regularization model was proposed for compressive sensing image reconstruction. ALM and ADMM methods were used to solve this model. Our proposed algorithm makes the fractional-order and the high-order total variation complement each other on image reconstruction. It can solve the problem of non-smooth in smooth areas when fractional-order total variation can enhance image edges and textures. In addition, it also addresses high-order total variation alleviates the staircase artifact produced by traditional total variation, still smoothes the details of the image and the effect is not ideal. Meanwhile, the proposed algorithm suppresses painting-like effects produced by nonlocal means regularization. Experimental results show that, comparing with several state-of-the-art algorithms, the reconstructed images obtained by the proposed approach not only outperformed many existing methods in terms of PSNR and SSIM but also had better visual quality.

Author Contributions: Conceptualization, L.H., resources, Y.Q. and H.Z. validation, Z.P. and J.M., supervision, Y.H. Writing—original draft, L.H.; Writing—review and editing Y.Q. and H.Z. All authors have read and agreed to the published version of the manuscript.

Funding: This work was supported by the National Natural Science Foundation of China (NSFC) (61675184 and 61405178).

Data Availability Statement: Not applicable.

Conflicts of Interest: The authors declare no conflict of interest.

Appendix A



Figure A1. Five additional test images.

Table A1. The table of experimental results the PSNR (dB)/SSIM of five additional test images.

Image	Algorithms	Measurement Rates				
		0.1	0.15	0.2	0.25	0.3
Woman	TV-NLR	28.406/0.804	29.886/0.847	31.261/0.877	32.540/0.901	33.325/0.917
	MH-BCS	28.610/0.825	30.779/0.813	31.624/0.890	33.175/0.911	34.141/0.921
	BCS-TV	27.982/0.781	29.581/0.829	30.766/0.858	31.914/0.882	32.74/0.901
	BCS-SPL	27.560/0.774	28.869/0.814	30.117/0.843	31.202/0.864	32.201/0.880
	TVAL3	27.259/0.781	29.539/0.835	30.786/0.863	31.880/0.887	32.941/0.904
	HoFrTV	29.099/0.832	31.130/0.878	32.241/0.901	33.342/0.916	34.555/0.931
Candy	TV-NLR	28.645/0.905	30.659/0.933	32.859/0.954	34.560/0.966	36.488/0.976
	MH-BCS	28.656/0.891	31.161/0.925	32.643/0.940	34.158/0.954	35.229/0.962
	BCS-TV	27.458/0.881	29.729/0.919	31.659/0.943	33.465/0.959	35.209/0.969
	BCS-SPL	26.467/0.842	28.283/0.877	30.261/0.901	31.242/0.919	32.352/0.932
	TVAL3	26.238/0.854	29.598/0.917	31.184/0.938	32.907/0.955	34.333/0.966
	HoFrTV	30.266/0.929	32.671/0.953	34.671/0.968	36.288/0.975	37.970/0.982
Bell	TV-NLR	25.070/0.846	26.858/0.883	28.615/0.912	29.682/0.927	31.401/0.943
	MH-BCS	25.262/0.826	26.275/0.864	28.666/0.898	29.861/0.916	30.838/0.928
	BCS-TV	23.937/0.795	25.619/0.847	27.044/0.883	28.276/0.905	29.621/0.923
	BCS-SPL	23.755/0.774	24.928/0.805	26.493/0.841	27.402/0.851	27.750/0.879
	TVAL3	23.469/0.775	25.899/0.861	27.538/0.895	28.915/0.914	30.194/0.929
	HoFrTV	25.758/0.860	27.827/0.897	29.381/0.920	30.862/0.935	32.229/0.948
Couple	TV-NLR	25.424/0.676	27.417/0.759	28.298/0.798	28.994/0.827	30.216/0.861
	MH-BCS	24.961/0.667	26.805/0.749	28.089/0.795	28.890/0.823	30.146/0.855
	BCS-TV	24.376/0.625	26.153/0.702	27.394/0.756	28.537/0.798	29.592/0.834
	BCS-SPL	23.773/0.580	24.933/0.632	25.827/0.673	26.57/0.7063	27.286/0.736
	TVAL3	23.426/0.615	26.081/0.719	27.745/0.774	28.911/0.816	30.117/0.848
	HoFrTV	25.765/0.695	27.589/0.774	29.323/0.828	30.553/0.864	31.728/0.891
Man	TV-NLR	23.469/0.632	24.775/0.707	25.972/0.754	26.810/0.790	27.875/0.828
	MH-BCS	23.328/0.624	24.856/0.701	25.920/0.748	26.860/0.784	27.564/0.808
	BCS-TV	22.902/0.596	24.483/0.681	25.593/0.737	26.628/0.779	27.543/0.816
	BCS-SPL	21.889/0.505	22.955/0.562	23.815/0.611	24.587/0.651	25.260/0.687
	TVAL3	22.327/0.567	23.211/0.619	24.35/0.678	25.206/0.720	27.504/0.811
	HoFrTV	23.754/0.660	25.4822/0.741	26.719/0.793	27.761/0.826	28.748/0.855

References

1. Donoho, D.L. Compressed sensing. *IEEE Trans. Inf. Theory* **2006**, *52*, 1289–1306. [\[CrossRef\]](#)
2. Candès, E.J.; Wakin, M.B.; Wakin, M.B. An introduction to compressive sampling. *IEEE Signal Process. Mag.* **2008**, *25*, 21–30. [\[CrossRef\]](#)
3. Duarte, M.F.; Davenport, M.A.; Takhar, D.; Laska, J.N.; Sun, T.; Kelly, K.F.; Baraniuk, R.G. Single-Pixel Imaging via Compressive Sampling. *IEEE Signal Process. Mag.* **2008**, *25*, 83–91. [\[CrossRef\]](#)
4. Alonso, M.T.; Dekker, P.L.; Mallorqui, J.J. A Novel Strategy for Radar Imaging Based on Compressive Sensing. *IEEE Trans. Geoelectron Remote Sens.* **2011**, *48*, 4285–4295. [\[CrossRef\]](#)

5. Lustig, M.; Donoho, D.L.; Santos, J.M.; Pauly, J.M. Compressed sensing MRI. *IEEE Signal Process. Mag.* **2008**, *25*, 72–82. [\[CrossRef\]](#)
6. Candès, E.J. The restricted isometry property and its implications for compressed sensing. *C. R.-Math.* **2008**, *346*, 589–592. [\[CrossRef\]](#)
7. Mutgekar, M.B.; Bhaskar, P.C. Analysis of DCT and FAST DCT using soft core processor. In Proceedings of the 2019 3rd International Conference on Trends in Electronics and Informatics (ICOEI), Tirunelveli, India, 23–25 April 2019; pp. 1128–1132. [\[CrossRef\]](#)
8. Rousset, F.; Ducros, N.; Farina, A.; Valentini, G.; D’Andrea, C.; Peyrin, F. Adaptive Basis Scan by Wavelet Prediction for Single-Pixel Imaging. *IEEE Trans. Comput. Imaging* **2017**, *3*, 36–46. [\[CrossRef\]](#)
9. Beck, A.; Teboulle, M. Fast Gradient-Based Algorithms for Constrained Total Variation Image Denoising and Deblurring Problems. *IEEE Trans. Image Process.* **2009**, *18*, 2419–2434. [\[CrossRef\]](#)
10. Iordache, M.-D.; Bioucas-Dias, J.M.; Plaza, A. Variation Spatial Regularization for Sparse Hyperspectral Unmixing. *IEEE Trans. Geosci. Remote Sens.* **2012**, *50*, 4484–4502. [\[CrossRef\]](#)
11. Li, C.; Yin, W.; Jiang, H.; Zhang, Y. An efficient augmented lagrangian method with applications to total variation minimization. *Comput. Optim. Appl.* **2013**, *56*, 507–530. [\[CrossRef\]](#)
12. Candès, E.J.; Wakin, M.B.; Boyd, S.P. Enhancing Sparsity by Reweighted L1 Minimization. *J. Fourier Anal. Appl.* **2007**, *14*, 877–905. [\[CrossRef\]](#)
13. Xu, J.; Ma, J.; Zhang, D.; Zhang, Y.; Lin, S. Improved total variation minimization method for compressive sensing by intra-prediction. *Signal Process.* **2012**, *92*, 2614–2623. [\[CrossRef\]](#)
14. Bredies, K.; Kunisch, K.; Pock, T. Total Generalized Variation. *Siam J. Imaging Sci.* **2010**, *3*, 492–526. [\[CrossRef\]](#)
15. Florian, K.; Bredies, K.; Pock, T.; Stollberger, R. Second order total generalized variation (TGV) for MRI. *Magn. Resonance Med.* **2010**, *65*, 480–491. [\[CrossRef\]](#)
16. Yang, J.; Zhang, Y.; Yin, W. A Fast Alternating Direction Method for TVL1-L2 Signal Reconstruction From Partial Fourier Data. *IEEE J. Sel. Top. Signal Process.* **2010**, *4*, 288–297. [\[CrossRef\]](#)
17. Guo, W.; Qin, J.; Yin, W. A New Detail-Preserving Regularization Scheme. *Siam J. Imaging Sci.* **2014**, *7*, 1309–1334. [\[CrossRef\]](#)
18. Zhang, J.; Liu, S.; Xiong, R.; Ma, S.; Zhao, D. Improved total variation based image compressive sensing recovery by nonlocal regularization. In Proceedings of the 2013 IEEE International Symposium on Circuits and Systems (ISCAS), Beijing, China, 19–23 May 2013; pp. 2836–2839. [\[CrossRef\]](#)
19. Jun, Z.; Zhihui, W. A class of fractional-order multi-scale variational models and alternating projection algorithm for image denoising. *Appl. Math. Model.* **2011**, *35*, 2516–2528. [\[CrossRef\]](#)
20. Tian, D.; Xue, D.Y.; Wang, D.H. A fractional-order adaptive regularization primal-dual algorithm for image denoising. *Inf. Sci.* **2015**, *296*, 147–159. [\[CrossRef\]](#)
21. Chen, H.; Qin, Y.; Ren, H.; Chang, L.; Hu, Y.; Zheng, H. Adaptive Weighted High Frequency Iterative Algorithm for Fractional-Order Total Variation with Nonlocal Regularization for Image Reconstruction. *Electronics* **2020**, *9*, 1103. [\[CrossRef\]](#)
22. Adam, T.; Paramesran, R. Image denoising using combined higher order non-convex total variation with overlapping group sparsity. *Multidimens. Syst. Signal Process.* **2019**, *30*, 503–527. [\[CrossRef\]](#)
23. Liu, P. Hybrid higher-order total variation model for multiplicative noise removal. *IET Image Process.* **2020**, *14*, 862–873. [\[CrossRef\]](#)
24. Mei, J.J.; Huang, T.Z. Primal-dual splitting method for high-order model with application to image restoration. *Appl. Math. Model.* **2015**, S0307904X15006022. [\[CrossRef\]](#)
25. Tang, L.; Ren, Y.; Fang, Z.; He, C. A generalized hybrid nonconvex variational regularization model for staircase reduction in image restoration. *Neurocomputing* **2019**, *359*, 15–31. [\[CrossRef\]](#)
26. Yang, J.-H.; Zhao, X.-L.; Ma, T.-H.; Chen, Y.; Huang, T.-Z.; Ding, M. Remote sensing images destriping using unidirectional hybrid total variation and nonconvex low-rank regularization. *J. Comput. Appl. Math.* **2020**, *363*, 124–144. [\[CrossRef\]](#)
27. Zhang, J.; Chen, K. Variational image registration by a total fractional-order variation model. *J. Comput. Phys.* **2015**, *293*, 442–461. [\[CrossRef\]](#)
28. Li, C. An Efficient Algorithm for Total Variation Regularization with Applications to the Single Pixel Camera and Compressive Sensing. Master’s Thesis, Rice University, Houston, TX, USA, 2010. Available online: <https://hdl.handle.net/1911/62229> (accessed on 1 September 2009).
29. Wang, Z.; Bovik, A.C.; Sheikh, H.R.; Simoncelli, E.P. Image quality assessment: From error visibility to structural similarity. *IEEE Trans. Image Process.* **2004**, *13*, 600–612. [\[CrossRef\]](#)
30. Mun, S.; Fowler, J.E. Block Compressed Sensing of Images Using Directional Transforms. In Proceedings of the 2010 Data Compression Conference, Snowbird, UT, USA, 24–28 March 2010; p. 547. [\[CrossRef\]](#)
31. Chen, C.; Tramel, E.W.; Fowler, J.E. Compressed-sensing recovery of images and video using multihypothesis predictions. In Proceedings of the 2011 Conference Record of the Forty Fifth Asilomar Conference on Signals, Systems and Computers (ASILOMAR), Pacific Grove, CA, USA, 6–9 November 2011; pp. 1193–1198. [\[CrossRef\]](#)